INVITED PAPER *Special Section on Opto-electronics and Communications for Future Optical Network*

Development of a 64 Gbps Si Photonic Crystal Modulator

Yosuke HINAKURA[†], ***Nonmember***, **Hiroyuki ARAI**[†], ***Fellow***, ***and*** **Toshihiko BABA**[†a)], ***Member***

SUMMARY A compact silicon photonic crystal waveguide (PCW) slow-light modulator is presented. The proposed modulator is capable of achieving a 64 Gbps bit-rate in a wide operating spectrum. The slow-light enhances the modulation efficiency in proportion to its group index n_g. Two types of 200-μm-long PCW modulators are presented. These are low- and high-dispersion devices, which are implemented using a complementary metal-oxide-insulator process. The lattice-shifted PCW achieved low-dispersion slow-light and exhibited $n_g \approx 20$ with an operating spectrum $\Delta\lambda \approx 20$ nm, in which the fluctuation of the extinction ratio is ±0.5 dB. The PCW device without the lattice shift exhibited high-dispersion, for which a large or small value of n_g can be set on demand by changing the wavelength. It was found that for a large n_g, the frequency response was degraded due to the electro-optic phase mismatch between the RF signals and slow-light even for such small-size modulators. Meander-line electrodes, which bypass and delay the RF signals to compensate for the phase mismatch, are proposed. A high cutoff frequency of 55 GHz was theoretically predicted, whereas the experimentally measured value was 38 GHz. A high-quality open eye pattern for a drive voltage of 1 V at 32 Gbps was observed. The clear eye pattern was maintained for 50–64 Gbps, although the drive voltage increased to 3.5–5.3 V. A preliminary operation of a 2-bits pulse amplitude modulation up to 100 Gbps was also attempted.

key words: *photonic crystal, optical modulator, silicon photonics*

1. Introduction

In recent years, large scaling and capacity enlargement of data centers have been progressing according to the growth of cloud services. The optical interconnects and silicon (Si) photonics complementary metal-oxide-semiconductor (CMOS) processes along with silicon-on-insulator (SOI) have become key technologies. IEEE802.3bs [1] defines optical transceivers specifications for the 400 Gbps Ethernet, such as 2 symbols × 50 Gbaud × 4 lanes, for a 500 m range. Using direct modulation of vertical-cavity surface-emitting lasers and transmission through multi-mode fibers (which are the major technologies at present) to achieve such high bit rates and distances will be a difficult task. On the other hand, Si photonics transceivers with external modulators and single-mode fibers provide a more advantageous solution.

Next, we focus on fast Si modulators. Optical interconnects require compact size, low operating voltage and power consumption, and low optical loss, as well as high-speed. In general, the downsizing of the devices contributes to a free layout and power saving in Si photonics. However, when Si is directly used as a phase-shifting material, its small carrier plasma dispersion (which is the operation principle of Si modulators) essentially results in a size and performance constraint [2]; in standard Si rib-waveguide Mach-Zehnder modulators (MZMs), a phase-shifter length L must be as long as several millimeters to obtain a sufficient high-speed phase shift using a CMOS-compatible drive voltage of $V_{pp} \leq 2$ V [3]–[10].

One approach to break this constraint is to use other materials formed on SOI, such as III-V semiconductors [11], [12], plasmonic materials [13], $LiNbO_3$ [14], and electro-optic (EO) polymers [15]. These materials are attractive because of their enhanced carrier plasma dispersion, enhanced optical confinement, or purely linear response of the Pockels effect with no absorption loss. However, these materials have the disadvantage of reduced CMOS compatibility and reliability. Another approach is to load an optical resonance structure in Si modulators. For example, a micro-ring achieves a footprint of a < 10 μm radius [10], [16]–[18]. However, their operating spectrum of 0.1 nm order is too narrow to be used in data centers without precise temperature control. This problem has hampered their practical use in optical interconnects. Another choice is a slow-light structure that balances the size, operating spectrum, and performance [19].

Slow-light with a small group velocity v_g (or large group index $n_g \equiv c/v_g$ for the vacuum light velocity c) and a desired operating spectrum $\Delta\lambda$ enhances any linear and nonlinear light-matter interactions. It can be easily generated in a photonic crystal waveguide (PCW) and has been applied in Si MZMs phase shifters, as depicted in Fig. 1 (a) [19]–[22]. Here, the phase shift $\Delta\phi$ is expressed as

$$\Delta\phi = k_0 n_g \frac{\Delta n_{eq}}{n_{eq}} L, \tag{1}$$

where k_0 is the wavenumber in vacuum, and Δn_{eq} is the equivalent modal index change induced by the material index change due to carrier plasma dispersion, for example. The above equation shows that $\Delta\phi$ increases in proportion to n_g and that L can be reduced by a large n_g for the desired $\Delta\phi$.

Our group has fabricated Si PCW MZM modulators and observed their operation at bit rates of 10–32 Gbps. In these studies, a phase shifter of length $L = 200$ μm was employed. This length is one-tenth of a rib-waveguide Si MZM's with $n_g \approx 4$. Although the PCW is a kind

Manuscript received December 25, 2019.
Manuscript revised April 20, 2020.
Manuscript publicized June 15, 2020.

[†]The authors are with Yokohama National University, Yokohama-shi, 240–8501 Japan.
a) E-mail: baba-toshihiko-zm@ynu.ac.jp

DOI: 10.1587/transele.2019OCP0004

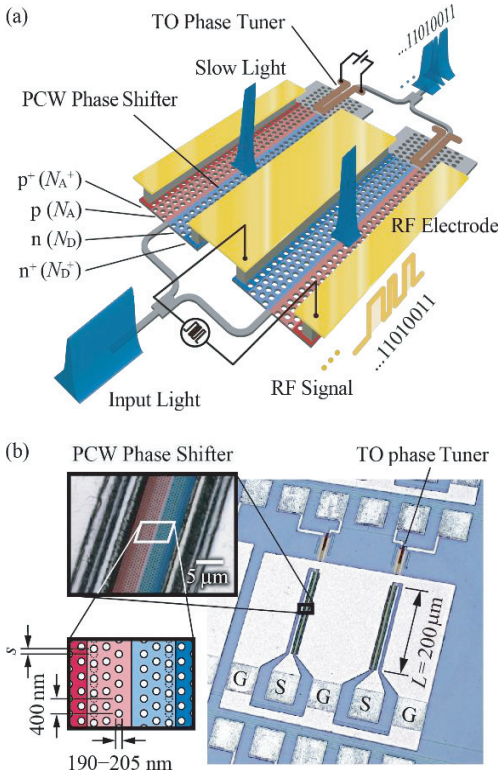

Fig. 1 Si PCW MZM. (a) Schematic diagram. (b) Fabricated device.

of optical resonance structures, its operating spectrum $\Delta\lambda$ can be moderately widened by photonic band engineering. The typical values of n_g and $\Delta\lambda$ are 15–25 and 15–20 nm, respectively, in a lattice-shifted PCW (LSPCW), which is designed to exhibit low-dispersion slow-light [23]. The large $\Delta\lambda$ allows wide temperature tolerance, and athermal operation has actually been observed in the range 19–124°C. In addition to the on-off-keying modulation, advanced modulation schemes for wavelength division multiplexing (WDM) [24] and multi-bit transmission [25] have also been demonstrated.

In this paper, the operational speed-up improvement in Si PCW MZMs is specifically discussed. Since slow light has an n_g much larger than that of RF signals, the frequency response is degraded by their phase mismatch, even though the device is very small. The mismatch can be compensated by employing an RF delay line called *meander-line* and optimizing the electrical termination. In Sect. 2, a review of the fabrication, transmission, and modulation characteristics of the MZMs with the LSPCW or PCW without lattice shifts is presented. These devices exhibit low- and high-dispersion slow light and are suitable for obtaining a wide operating spectrum. Also, n_g can be set to the desired value by changing the wavelength. In Sect. 3, the frequency response, which is affected by the phase mismatch (particularly for a large n_g) and its compensation, is discussed. In Sect. 4, high-speed operation up to 64 Gbps, as well as preliminary pulse amplitude modulation (PAM-4) up to 100 Gbps, is demonstrated.

2. Fabrication, Transmission, and Modulation

2.1 Fabrication

The device was fabricated on a 200-mm-diameter SOI with a Si slab thickness of 210 nm using a CMOS process with KrF excimer laser lithography at $\lambda = 248$ nm with phase shift masks, as shown in Fig. 1 (b). The LSPCW/PCW consists of a single line defect in a triangular lattice array of holes buried by SiO_2 cladding. The diameter $2r$ was designed to be 190–220 nm, and the lattice constant $a = 400$ nm to achieve operation at C band ($\lambda = 1530$–1565 nm). The phase shifters of $L = 200$ μm consist of the LSPCW or PCW with a p-n junction. In the LSPCW, a lattice shift s of 95 nm was set at the third rows of holes from the line defect. As reported in detail [23], this arrangement produces low-dispersion slow-light with $n_g \approx 20$ and $\Delta\lambda \approx 20$ nm. Regarding the p-n junction, an interleaved profile was employed in the experiment described in Sect. 2.2 to achieve a large $\Delta\phi$, whereas a linear profile was used in the later sections to investigate high speeds. In the interleaved junction, the period and depth of the interleave profile were both set at 600 nm. For the p- and n-dopings, different concentrations were tested, i.e., $N_A = 9.5\times10^{17}$ cm^{-3} and $N_D = 5.7\times10^{17}$ cm^{-3}, respectively, for the experiment described in Sect. 2.2; 4.8×10^{17} cm^{-3} and 4.8×10^{17} cm^{-3}, respectively, in Sect. 2.3; 10.5×10^{17} cm^{-3} and 6.2×10^{17} cm^{-3}, respectively, in Sect. 3. The highly doped regions outside the p-n junction were used to implement ohmic contacts. They were placed 4 μm apart to avoid the absorption of the guided slow-light mode. Al electrodes were employed for the signal (S) and ground (G) contacts in a G-S-G-S-G coplanar configuration. As shown in Fig. 1 (b) and discussed in detail in Sect. 3.1, the G probing pads were commonized to suppress the unbalanced RF transmission due to the coupled slotline mode. The half-wave voltage-length product $V_\pi L$ of this phase shifter was estimated to be 0.23 V·cm and 0.13 V·cm for the linear and interleaved p-n junction, respectively, for the doping concentrations of $N_A = 10.5\times10^{17}$ cm^{-3} and $N_D = 6.2\times10^{17}$ cm^{-3}, and for $n_g = 22$ [20]. Since the $V_\pi L$ relationship with n_g is inversely proportional, $V_\pi L$ would be equal to 0.14, 0.11, and 0.08 V·cm for $n_g = 30$, 40, and 50, respectively. The $V_\pi L$ value increases for the lower doping concentrations of the high-dispersion devices in Sects. 2.2 and 2.3.

2.2 Low-Dispersion Device

The wide operating spectrum of the LSPCW device was investigated. An example transmission spectrum normalized by that of a reference Si-wire waveguide on the same chip is shown in Fig. 2 (a). The maximum transmittance was −5 dB, including a less than 0.2 dB loss for each of the two 1×2 multi-mode interference couplers in the MZ interferometer and a less than 0.5 dB loss for each of the two junctions between the Si-wire waveguide and LSPCW. The residual loss is caused by propagation in the LSPCW, where the

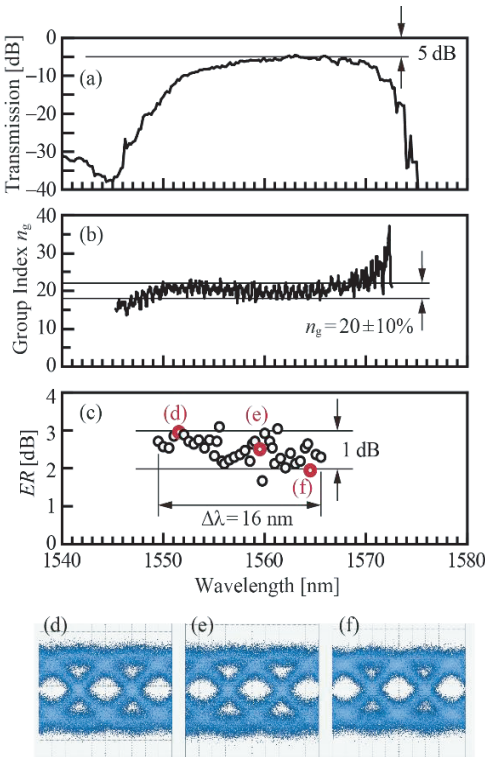

Fig. 2 Wide operating spectrum of the low-dispersion device. (a) Transmission spectrum. (b) n_g spectrum. (c) *ER* spectrum for modulation with V_{pp} = 1.75 V and V_{DC} = −0.9 V. (d)–(f) Eye patterns observed for (d) λ = 1551.5 nm, (e) λ = 1559.5 nm, and (f) λ = 1564.5 nm.

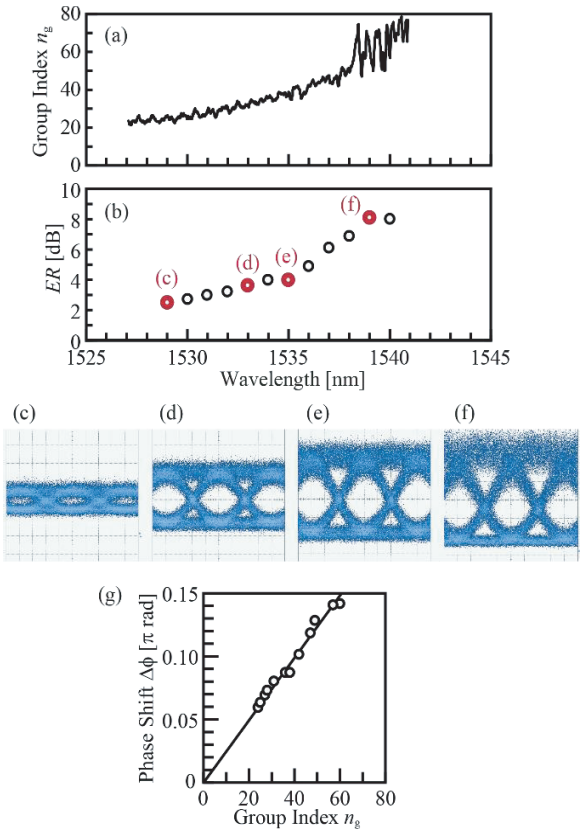

Fig. 3 n_g tuning in the high-dispersion device. (a) n_g spectrum. (b) *ER* spectrum for modulation with V_{pp} = 1.75 V and V_{DC} = −0.9 V. (c)–(f) Eye patterns observed for (c) λ = 1529 nm, (d) λ = 1533 nm, (e) λ = 1535 nm, and (f) λ = 1539 nm. Vertically asymmetric eyes in (e) and (g) were caused by the phase bias point below the quadrature point.

scattering loss caused by the disordering of the fabricated PCW was trivial, and the free carrier absorption was dominant. By performing further optimizations in the future, the losses other than the absorption are expected to become negligible, and the total on chip-loss is expected to be ~3 dB. The corresponding n_g spectrum is shown in Fig. 2 (b). The average n_g was 20 and the operating spectrum, which is defined so that the fluctuation in n_g is within ±10%, ranged from λ = 1548 to λ = 1569 nm ($\Delta\lambda$ = 21 nm). Neglecting the small oscillation due to the Fabry-Perot resonance in the LSPCW [26], the n_g spectrum appears to be almost flat except for the spectral edges.

By varying the wavelength in the range λ = 1549.5–1565.5 nm ($\Delta\lambda$ = 16 nm) with a 0.5-nm step, a 25-Gbps modulation was performed with non-return-to-zero (NRZ) pseudo-random bit sequence (PRBS) signals obtained from a pulse-pattern generator (PPG, Anritsu MP1800A). The two phase shifters were driven by a drive voltage V_{pp} = 2 V under a push-pull configuration with a bias voltage V_{DC} = −0.9 V. The phase bias of the MZM was controlled by thermo-optic phase tuners, considering the balance between the modulation efficiency and transmission loss. In this experiment, it was set up so that the average optical power was 2 dB below the maximum transmission power. The electrical termination was omitted to enhance modulation efficiency. The extinction ratio *ER* is shown in Fig. 2 (c). The corresponding eye patterns observed using a sampling oscilloscope (Keysight 86100C) are shown in Figs. 12 (d)–(f). The eye pattern opened almost equally for all wavelengths, and the *ER* was distributed within 2.5 ± 0.5 dB. This small *ER* value was mainly due to the low doping concentrations in this experiment, and as reported in [20], *ER* >3 dB is usually obtained for similar devices with moderately high doping concentrations. Higher n_g = 30–40 increases the *ER* margin; a LSPCW of such high n_g has been designed and fabricated, and higher modulation efficiency has been confirmed [23]. Such devices reduce the operating wavelength range to 12–18 nm, respectively. However, this is not considered as a drawback, when each wavelength range is limited in a wavelength division multiplexing system.

2.3 High-Dispersion Device

For the PCW without lattice shifts, n_g increases with the wavelength toward the band edge, as shown in Fig. 3 (a); n_g is 22 for λ = 1527 nm and ~80 for λ = 1541 nm. The modulation efficiency is lower than that of other experiments due to the low doping concentrations. In fact, it is enhanced by the larger n_g. A 25-Gbps modulation was observed by varying the wavelength by 1 nm in the range λ = 1529–1540 nm. The voltages were the same as those in the above experi-

ment, whereas the phase bias was varied so that the average optical power decreased from the maximum by 9 dB. The aim was to compensate for the low modulation efficiency due to the low doping concentrations. This resulted in the low signal-to-noise ratio of the eye patterns in this experiment. The observed *ER* spectrum and the eye patterns for different wavelengths are shown in Figs. 3 (b) and (c)–(f), respectively. The *ER* increased from 2.5 dB for $n_g = 25$ to 8.1 dB for $n_g = 64$. $\Delta\phi$, which was estimated from the *ER* is shown in Fig. 3 (g). An almost linear relation with n_g is observed. This means that $\Delta n_{eq}/n_{eq}$ in Eq. (1) is almost unchanged in this range.

3. Frequency Response

3.1 Suppression of the Coupled Slotline Mode

The RF frequency response of the PCW MZM with probing pads for both input and output was measured using a vector network analyzer (Anritsu 37962E-R) by driving the single arm of the device. The black lines in The S_{11} and S_{21} parameters, i.e., the reflection and transmission spectra of the RF signals, respectively, when the G electrodes were not commonized on the chip, are presented in Fig. 4 (a). The S_{11} and S_{21} curves exhibited a slow peak and valley at $f \approx 20$ GHz, respectively. These are considered to be caused by a coupled slotline mode, which is excited by the unbalanced electrical potentials between the G electrodes [27]–[29]. This mode was suppressed by the commonization shown in Fig. 1 (b). The red lines shown in Fig. 4 (a) are those after commonization. The peak and valley disappeared and the curves become smoother. The improvement was more obvious when the EO frequency response was measured by adding an OE converter of a greater than 70 GHz bandwidth to the network analyzer. In the uncommonized device, the response decreased sharply at $f = 15$–23 GHz due to the influence of the coupled slotline mode. In the commonized device, the sharp decrease was suppressed and the response became smoother.

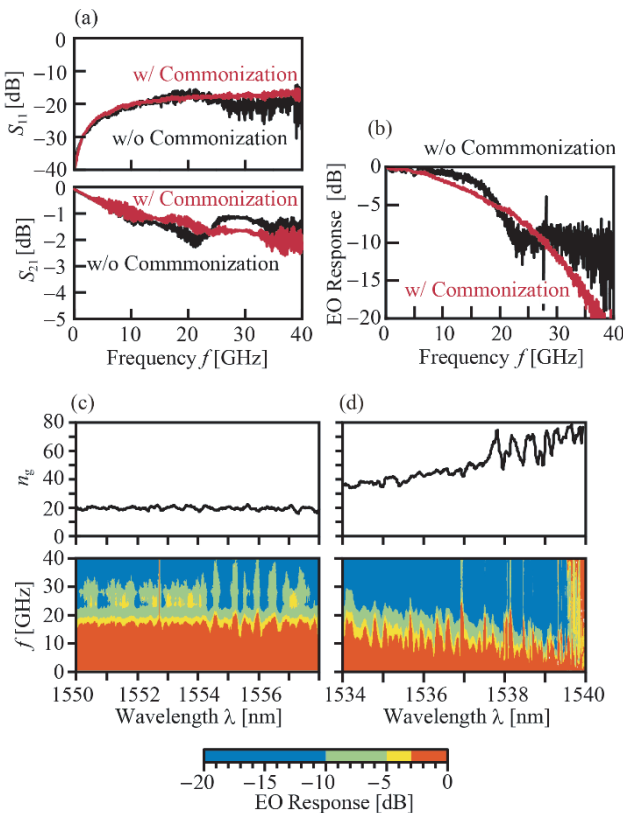

Fig. 4 Measured frequency response of the normal electrode devices. (a) Electrical response with and without G electrode commonization. (b) EO response with and without commonization, when $n_g = 20$ and $V_{DC} \approx -2$ V. (c) n_g spectrum and frequency response map of the low-dispersion device. (d) n_g spectrum and frequency response map of the high-dispersion device.

This suppression enabled us to further investigate a crucial factor related with the modulation speed. In the proposed device, the cutoff frequency f_{3dB} was as low as 14 GHz even after the commonization. In a finite element simulation [20], the obtained resistance R_{pn} and capacitance C_{pn} values of the linear p-n junction were 60 Ω and 50 fF, respectively. Therefore, an $f_{3dB} = 28.9$ GHz from $1/2\pi(R_{pn} + Z_g)C_{pn}$ was expected with a driver impedance $Z_g = 50$ Ω. The lower value obtained from the experiment indicates the existence of a dominant factor other than the RC time constant.

3.2 Phase Mismatch

The frequency response of the low- and high-dispersion devices was measured by varying the wavelength with a 0.02 nm step. The results were mapped as color plots in Figs. 4 (c) and (d). The boundary between the red and yellow areas indicates the cutoff frequency f_{3dB}. The low-dispersion device exhibited an almost flat spectrum with $f_{3dB} \approx 18$ GHz. On the other hand, the high-dispersion device exhibited a gradually decreasing f_{3dB} toward the long wavelength; $f_{3dB} \approx 15$ GHz for $n_g \approx 35$ at $\lambda = 1534$ nm, and $f_{3dB} \approx 5$ GHz for $n_g \approx 75$ at $\lambda = 1540$ nm. Thus, the response appeared to depend on n_g. This result can be explained by the phase mismatch (or velocity mismatch) between the RF signals and slow light; the PCW MZM behaves as a distributed constant device even though its length is as short as 200 μm.

For $LiNbO_3$ and III-V semiconductor MZMs, which have a long history of development up to their present commercial use, the phase matching issue has been fully studied, since their phase shifter is quite long (order of millimeter to centimeter). This issue severely constrains the frequency response, although the mismatch is small [30]–[35]. The phase matching issue has also been studied for Si modulators [36], [37]. With reference to these works, the behavior of the PCW MZMs was analyzed as follows. The average voltage applied to the p-n junction, V_{ave}, is given by [22]

$$V_{ave}(f) = \frac{Z_0 V_g \left(e^{j\varphi_+} \operatorname{sinc} \phi_+ + \Gamma_L e^{j\varphi_-} e^{-2\gamma L} \operatorname{sinc} \phi_- \right)}{(Z_0 + Z_g)(1 - \Gamma_g \Gamma_L e^{-2\gamma L})} \quad (2)$$

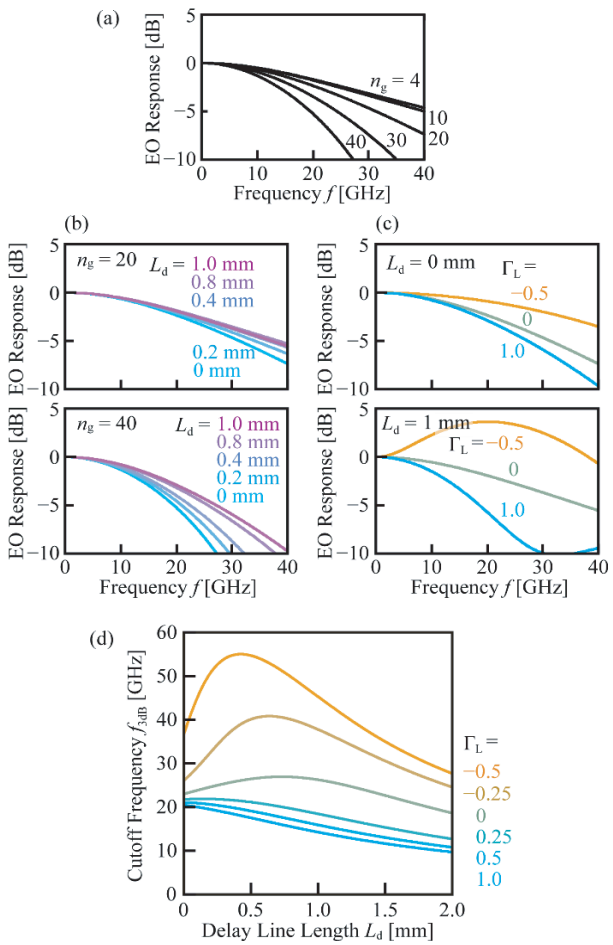

Fig. 5 Calculated frequency response. (a) n_g dependence. (b) L_d dependence. (c) Γ_L dependence. (d) f_{3dB} versus L_d for different Γ_L.

$$\varphi_{\pm} = \frac{(\beta_{SL} \pm j\gamma)L}{2} \tag{3}$$

$$\gamma = \alpha_{RF} + j\beta_{RF} = \alpha_{RF} + j\frac{2\pi f n_{RF}}{c} \tag{4}$$

where Z_0 is the characteristic impedance of the phase shifter, V_g is the output voltage from the signal generator, Γ_g and Γ_L are the RF reflection coefficients at the signal generator and the termination resistor, respectively, $\beta_{SL} = 2\pi f n_g/c$ is the propagation constant of the modulated slow-light signals, α_{RF} is the attenuation constant of the RF signals, and β_{RF} is the propagation constant of the RF signals. In the absence of the load resistor, the EO response is expressed as

$$S_{21}(f)\,[\mathrm{dB}] = 20\log_{10}\left|\frac{V_{ave}(f)G(f)}{V_{ave}(0)G(0)}\right| \tag{5}$$

$$G(f) = 1/[1 + j\,2\pi f(Z_g + R_{pn})C_{pn}] \tag{6}$$

The calculated response for different values of n_g is presented in Fig. 5, where $\Gamma_g = \Gamma_L = 0$, $n_{RF} = 4$, and the other parameters are the same as those noted above. When $\alpha_{RF} = 0$ and $n_g = 4$ (phase matching condition), the response is determined only by $G(f)$ and $f_{3dB} = 28.9$ GHz, as already mentioned. This value decreases to 15.1 GHz when

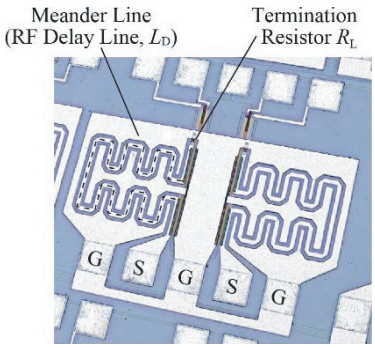

Fig. 6 Fabricated meander-line electrode device of $L_d = 1086\ \mu$m.

n_g increases to 40. Thus, the frequency response affected by the phase mismatch can be theoretically predicted even when the device's length is only 200 μm.

3.3 Compensation Using a Meander-Line Electrode

To compensate for the phase mismatch, meander-line electrodes were inserted into two separate sections of each phase shifter, as shown in Fig. 6. In the first section, slow light and RF signals co-propagate, shifting each phase. Then, the RF signals enter the meander-line of length L_d. After the advanced phase is delayed in the meander-line, the RF signals enter the second section so that they co-propagate with the slow light again.

With the meander-line, the expression for V_{ave} is modified as [19]

$$V_{ave}(f) = \frac{Z_0 V_g \left\{ \begin{array}{l} \left(e^{\frac{j\varphi_+}{2}} + e^{\frac{j3\varphi_+}{2} - j\varphi_d}\right)\mathrm{sinc}\,\dfrac{\varphi_+}{2} \\ + \Gamma_L e^{-2\gamma L}\left(e^{\frac{j\varphi_-}{2} - 2j\varphi_d} + e^{\frac{j3\varphi_-}{2} - j\varphi_d}\right)\mathrm{sinc}\,\dfrac{\varphi_-}{2} \end{array} \right\}}{2(Z_0 + Z_g)(1 - \Gamma_g\Gamma_L e^{-2\gamma L - j\,2\varphi_d})} \tag{7}$$

$$\varphi_d = \frac{2\pi f n_d L_d}{c} \tag{8}$$

where n_d is the equivalent modal index of the RF signals in the meander-line. The calculated frequency response for different values of L_d is presented in Fig. 5 (b). For $n_g = 20$, the response is improved as L_d increases from 0 mm to 0.8 mm, but it is rather degraded for $L_d = 1.0$ mm, meaning that the phase mismatch becomes large again. For $n_g = 40$, the response is simply improved, when L_d becomes longer.

Γ_L also affects the response greatly, since the slow light in the phase shifter is modulated not only by the forward propagating RF signals but also by the backward ones. Depending on their phase relationship, the modulation by the forward wave is strengthened or canceled by the backward wave. Even without reactance components, Γ_L can be a negative value that cancels the forward wave. The calculated response for different Γ_L is presented in Fig. 5 (c). When $L_d = 0$ mm, the response is simply improved by a negative Γ_L, since the low-frequency components are particularly

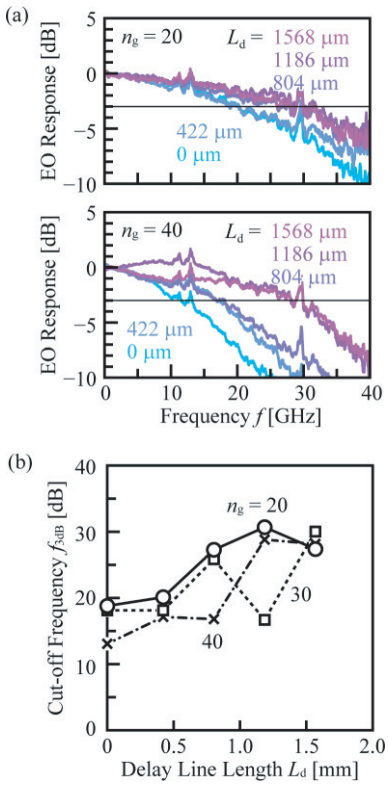

Fig. 7 (a) Measured frequency response for different L_d with $R_L = 50\ \Omega$ and $V_{DC} = -2$V. (b) Measured f_{3dB} versus L_d for $R_L = 50\ \Omega$ and different n_g.

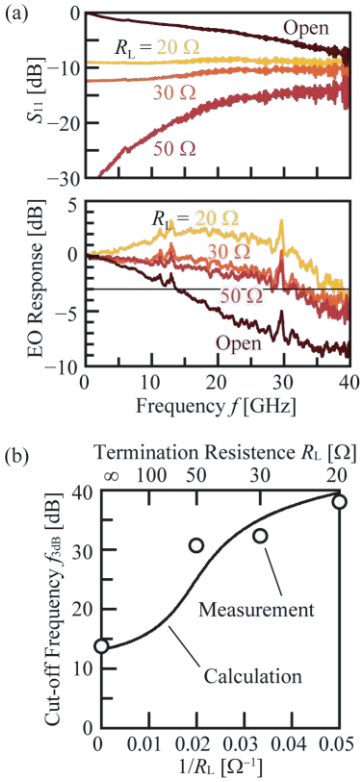

Fig. 8 (a) Measured frequency response for the meander-line device with $L_d = 1086\ \mu$m and different R_L. (b) f_{3dB} measured and calculated with $1/R_L$ for $n_g = 20\ \Omega$ and $L_d = 1186\ \mu$m.

canceled, and the high frequency components are relatively strengthened. When $L_d = 1.0$ mm, the response around 20 GHz is particularly strengthened for $\Gamma_L = -0.5$. The L_d dependence of f_{3dB} for different values of Γ_L is summarized in Fig. 5 (d). The negative Γ_L improves the f_{3dB} significantly; a high f_{3dB} of 56 GHz and 40 GHz is estimated for $\Gamma_L = -0.5$ and -0.25, respectively, for the optimum L_d.

A fabricated PCW MZM with the linear p-n junction and meander-line electrode of $L_d = 1186\ \mu$m is shown in Fig. 6. Each delay line has the same G-S-G coplanar waveguide as that of the phase shifter. Devices of $L_d = 422$, 804, and 1568 μm were also prepared. In this experiment, the electrodes were terminated by TiN load resistors of $R_L = 20$, 30, or 50 Ω. The relation between R_L and Γ_L is expressed as

$$\Gamma_L = \frac{R_L - Z_0}{R_L + Z_0} \tag{9}$$

Since $Z_0 = 30$–40 Ω in a typical p-n junction Si phase shifter [7], [8], a negative Γ_L for $R_L \leq 30\ \Omega$ is expected. This device was fabricated in a different lot from the previous devices. Initially, the frequency response of the 50-Ω terminated devices was measured, as shown in Fig. 7 (a). As theoretically predicted, the frequency response was improved as L_d increased. This improvement appeard to be clearer for $n_g = 40$. The f_{3dB} variation with L_d was summarized in Fig. 7 (b). For each value of n_g, f_{3dB} was improved by increasing L_d. Its highest value reached 32 GHz for $L_d = 1186\ \mu$m. This L_d value requires an additional footprint, as shown in Fig. 6. However, since the footprint of the normal electrode device is already constrained by the electrode pads, the increase due to the meander-line electrodes is only 16%. This can be eliminated by narrowing the S electrodes and expanding the S-G gap, thus increasing the refractive index for the RF signals. Next, the frequency response dependence on the R_L was evaluated. The observed S_{11} and EO responses are presented in Fig. 8 (a). S_{11} was greater than −10 dB for the open device and decreases as R_L increases. It was particularly suppressed for $R_L = 50\ \Omega$, whereas it became higher for $R_L = 20$–30 Ω. This means that Γ_L approached zero at 50 Ω and became negative at 20–30 Ω. The EO response directly reflects S_{11} and was improved by a smaller R_L, as shown in Fig. 8 (b). For $R_L = 20\ \Omega$, the response around 20 GHz was strengthened similarly to the calculated result, and a high f_{3dB} of 38 GHz was observed. This result shows that the previously mentioned theoretical model well represents the behavior of the devices.

4. High-Speed Modulation

4.1 25 and 32 Gbps Modulation

Since f_{3dB} was much higher than that observed in Sect. 2 for the meander-line device with the negative Γ_L, significant im-

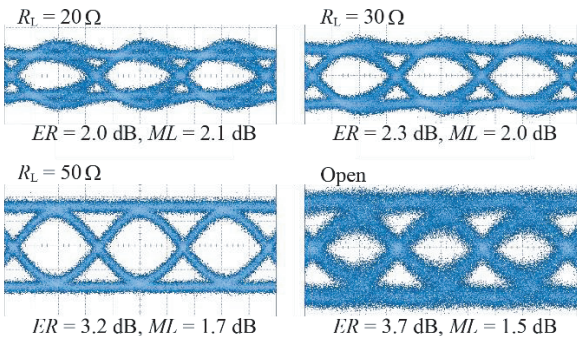

Fig. 9 32-Gbps eye patterns for $L_d = 1186\ \mu$m, $n_g = 30$, $V_{pp} = 2$ V, $V_{DC} = -1$ V, and different termination conditions.

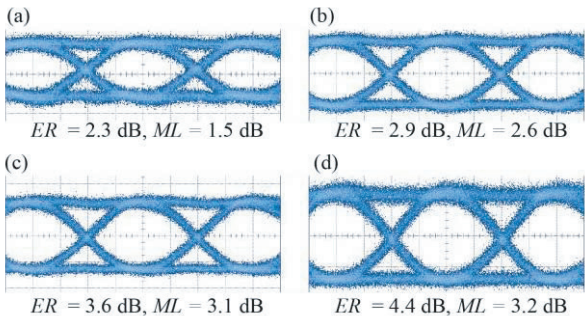

Fig. 10 25-Gbps eye patterns of the Si PCW MZM for $L_d = 1568\ \mu$m, $n_g = 40$, $V_{pp} = 1$ V, $V_{DC} = -0.5$ V, and different phase bias points. (a) Quadrature point. (b)–(d) Points at which the average transmission intensity decreases by 4 dB, 5 dB, and 6 dB, respectively, with respect to the maximum transmission power.

provement in the high-speed modulation characteristics was expected. The 32-Gbps eye patterns for a high-dispersion device exhibiting $n_g = 30$ at the quadrature point are shown in Fig. 9. Here, the modulation loss *ML* is defined as the attenuation of the "1"-level intensity of the eye pattern with respect to the maximum optical transmission intensity without modulation. For $R_L = 20$–$30\ \Omega$ and $L_d = 1186\ \mu$m, the high frequency components were relatively strengthened, so the fast transition from "0" or "1" level and vice versa exhibited the overshooting. For $R_L = 50\ \Omega$, the *ER* increased and a clearly open eye pattern was observed. For the open termination device, the *ER* achieved its maximum value due to the V_{ave}, which was increased by the RF reflection. However, the eye pattern became noisy and its rise and fall appeared to be slightly slowed.

The operating wavelength at which n_g increases to 40 was shifted, and the 50-Ω terminated device having the meander line of $L_d = 1568\ \mu$m was driven by V_{pp} and V_{DC} as low as 1 V and −0.5 V, respectively. The observed 25-Gbps eye patterns for four different points of the phase bias are shown in Fig. 10. Although *ER* was as small as 2.3 dB at the quadrature point, a clear eye pattern was observed, as shown Fig. 10 (a). The *ER* increased up to 4.4 dB, when the phase bias was increased, so that the average transmission decreased by 4 dB, 5 dB, and 6 dB, respectively, with respect to the maximum transmission power, as shown in

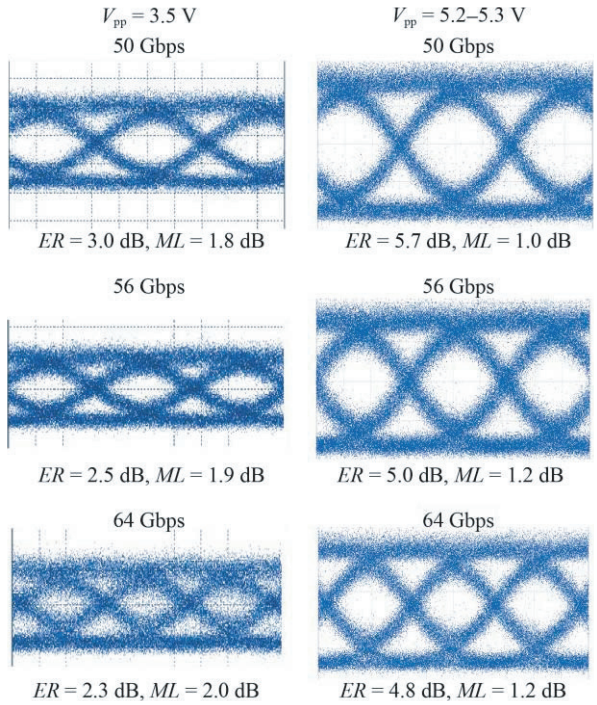

Fig. 11 50-, 56-, 64-Gbps eye patterns of Si PCW MZM for $V_{pp} = 3.5$ V, 5.2–5.3 V, and $V_{DC} = -3$ V.

Fig. 10 (b)–(d). For these experiments with $V_{pp} = 1$ V and 2 V, the dynamic bit energy consumption at the p-n junction ($C_{pn}V_{pp}/2$) is estimated to be 25 fJ/bit and 100 fJ/bit, respectively. The static power consumed by the 50-Ω resistors is estimated to be 10 mW and 40 mW, respectively.

4.2 50–64 Gbps Modulation

50-, 56-, and 64-Gbps NRZ PRBS signals were generated using a two-channel PPG, multiplexer (SHF 601A) and frequency equalizer (SHF EQ25-3 dB). The PPG voltage was amplified by RF amplifiers to $V_{pp} = 3.5$ V or 5.2–5.3 V. The 20-Ω terminated device was driven by these signals and $V_{DC} = -3$ V. The operation wavelength was set to $n_g = 20$, and the phase bias was set to the quadrature point. The eye patterns of the modulated light were observed by an optical sampling oscilloscope (Alnair labs, EYE-1000C), as shown in Fig. 11 (these patterns appear to be different from those in Figs. 9 and 10 because of the different oscilloscope used). For $V_{pp} = 3.5$ V, a clear eye pattern opened up to 56 Gbps with $ER = 2.5$–3.0 dB. However, it closed or became noisy at 64 Gbps due to unstable self-triggering in the oscilloscope. For $V_{pp} = 5.2$–5.3 V, the open eye pattern was maintained up to 64 Gbps with $ER \approx 5$ dB. The bit error rate *BER* estimated from the 50 Gbps eye pattern was 8.9×10^{-9}, which is close to the error-free condition. For $V_{pp} = 5.2$ V and $V_{DC} = -3$ V, the dynamic bit energy consumption at the p-n junction is still estimated to be as low as ∼0.7 pJ/bit, whereas the static power consumption increases to 900 mW. This large static power consumption is due to the high V_{DC} and low R_L. It is anticipated that it can be re-

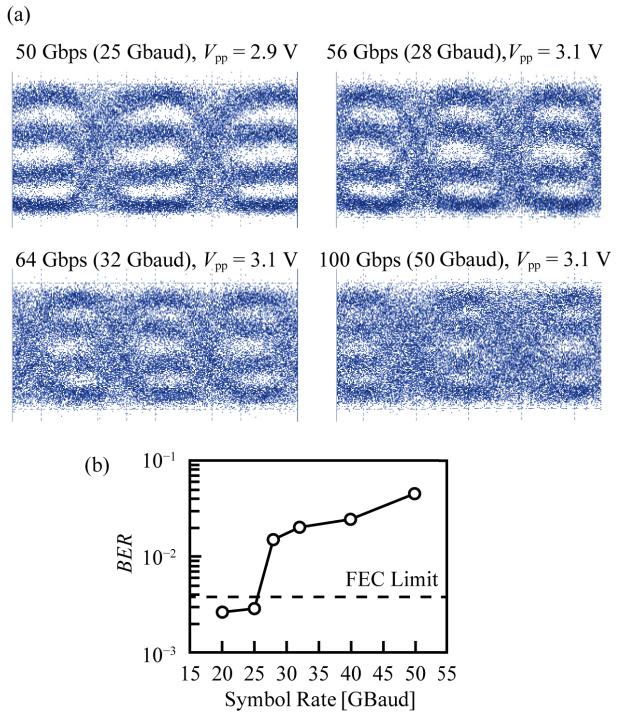

Fig. 12 PAM-4 eye patterns of Si PCW MZM for different symbol rates.

duced to < 310 mW by employing a larger n_g = 30–40 and a meander-line optimized for it.

4.3 Pulse Amplitude Modulation

PAM-4 modulation was also attempted on the same device by setting n_g = 20. The PAM-4 signals were generated using a 50 Gbps PPG (SHF 12103A) and a 3-bit digital-to-analog converter (SHF 613A). These signals were amplified to V_{pp} = 2.9–3.1 V after linear RF amplification with V_{DC} = −3 V. The observed eye patterns are shown in Fig. 12 (a). At 50 Gbps (25 Gbaud), a clear eye pattern was observed. The noise increased as the bit-rate increases. The eye shape was barely maintained up to 100 Gbps (50 Gbaud). The *BER* estimated from the Gaussian fitting to the plots of the eye patterns for different bit rates is shown in Fig. 12 (b). The *BER* was below the forward error correction limit of 3.8×10^{-3} [41] up to 25 Gbaud, but exceeded 10^{-2} at higher baud rates. It is known that 1.5-fold f_{3dB} is required against the baud rate in the PAM-4 operation. In this study, frequency equalization was only applied to the measurement system. Further improvement can be expected by the equalization, including the device.

5. Conclusions

By employing a low-dispersion design, the PCW slow-light MZM allowed a wide operating spectrum, which is equivalent to a wide temperature tolerance. The typical spectral width was 15–20 nm for n_g = 20 and the fluctuation of *ER* was ±0.5 dB. The phase shift in the MZM was linearly enhanced by n_g, whereas the phase mismatch degraded the frequency response for large values of n_g. By employing meander-line electrodes to delay the RF signals and a termination resistor that inverts the phase of RF reflection, the phase mismatch was well compensated, and the frequency response was significantly improved. The cutoff frequency f_{3dB} = 55 GHz was theoretically calculated, and f_{3dB} = 38 GHz was experimentally measured. In these devices, at 32-Gbps, a clear open eye pattern was observed for V_{pp} = 1 V. In addition, 50-, 56-, 64-Gbps eye patterns were confirmed for V_{pp} = 3.5–5.3 V. The preliminary PAM-4 operation at 50–100 Gbps (25–50 Gbaud) was also demonstrated.

If a CMOS driver is used, V_{pp} should be lower than 2 V [38]–[40]. In this study, the proposed device required V_{pp} > 3.5 V at 50 Gbps and beyond. n_g = 20 was used for this experiment. However, if n_g = 30–40 is used with an optimized meander-line length, V_{pp} will be reduced to 2.3–1.8 V, respectively. Thus, the dynamic bit energy consumption is also reduced to ∼100 fJ/bit, and the static power consumption can be reduced to ∼20 mW.

Acknowledgments

We appreciate Mr. Okitsu of SHF Japan Co., Ltd. and Mr. Takezawa of i-wave Co., Ltd. for using the equipment. This paper is based on results obtained from a project, JPNP13004, commissioned by the New Energy and Industrial Technology Development Organization (NEDO).

References

[1] IEEE Standard for Ethernet – "Amendment 10: Media Access Control Parameters, Physical Layers, and Management Parameters for 200 Gb/s and 400 Gb/s Operation," in IEEE Std 802.3bs-2017 (Amendment to IEEE 802.3-2015 as amended by IEEE's 802.3bw-2015, 802.3by-2016, 802.3bq-2016, 802.3bp-2016, 802.3br-2016, 802.3bn-2016, 802.3bz-2016, 802.3bu-2016, 802.3bv-2017, and IEEE 802.3-2015/Cor1-2017), pp.1–372, 12 Dec. 2017.

[2] R. Soref and B. Bennett, "Electrooptical effects in silicon," IEEE J. Quantum Electron., vol.23, no.1, pp.123–129, Jan. 1987.

[3] D.J. Thomson, F.Y. Gardes, J.-M. Fedeli, S. Zlatanovic, Y. Hu, B.P.P. Kuo, E. Myslivets, N. Alic, S. Radic, G.Z. Mashanovich, and G.T. Reed, "50-Gb/s Silicon Optical Modulator," IEEE Photon. Technol. Lett., vol.24, no.4, pp.234–236, Feb. 2012.

[4] M. Streshinsky, R. Ding, Y. Liu, A. Novack, Y. Yang, Y. Ma, X. Tu, E.K.S. Chee, A.E.-J. Lim, P.G.-Q. Lo, T. Baehr-Jones, and M. Hochberg, "Low power 50 Gb/s silicon traveling wave Mach-Zehnder modulator near 1300 nm," Opt. Express, vol.21, no.25, pp.30350–30357, Dec. 2013.

[5] X. Zhang, A. Hosseini, S. Chakravarty, J. Luo, A.K.-Y. Jen, and R.T. Chen, "Wide optical spectrum range, subvolt, compact modulator based on an electro-optic polymer refilled silicon slot photonic crystal waveguide," Opt. Lett., vol.38, no.22, pp.4931–4934, 2013.

[6] R. Ding, Y. Liu, Y. Ma, Y. Yang, Q. Li, A.E.-J. Lim, G.-Q. Lo, K. Bergman, T. Baehr-Jones, and M. Hochberg, "High-Speed Silicon Modulator With Slow-Wave Electrodes and Fully Independent Differential Drive," J. Light. Technol., vol.32, no.12, pp.2240–2247, June 2014.

[7] H. Xu, X. Li, X. Xiao, P. Zhou, Z. Li, J. Yu, and Y. Yu, "High-speed silicon modulator with band equalization," Opt. Lett., vol.39, no.16, pp.4839–4842, Aug. 2014.

[8] D. Patel, S. Ghosh, M. Chagnon, A. Samani, V. Veerasubramanian, M. Osman, and D.V. Plant, "Design, analysis, and transmission system performance of a 41 GHz silicon photonic modulator," Opt. Express, vol.23, no.11, pp.14263–14287, June 2015.
[9] A. Samani, M. Chagnon, D. Patel, V. Veerasubramanian, S. Ghosh, M. Osman, Q. Zhong, and D.V. Plant, "A Low-Voltage 35-GHz Silicon Photonic Modulator-Enabled 112-Gb/s Transmission System," IEEE Photon. J., vol.7, no.3, pp.1–13, June 2015.
[10] M. Pantouvaki, S.A. Srinivasan, Y. Ban, P. De Heyn, P. Verheyen, G. Lepage, H. Chen, J. De Coster, N. Golshani, S. Balakrishnan, P. Absil, and J. Van Campenhout, "Active Components for 50 Gb/s NRZ-OOK Optical Interconnects in a Silicon Photonics Platform," J. Light. Technol., vol.35, no.4, pp.631–638, Feb. 2017.
[11] T. Hiraki, T. Aihara, K. Hasebe, K. Takeda, T. Fujii, T. Kakitsuka, T. Tsuchizawa, H. Fukuda, and S. Matsuo, "Heterogeneously integrated III–V/Si MOS capacitor Mach–Zehnder modulator," Nature Photonics, vol.11, no.8, pp.482–485, Aug. 2017.
[12] M. Takenaka, S. Takahashi, S. Takagi, J.-H. Han, F. Boeuf, J.-K. Park, Q. Li, C.P. Ho, D. Lyu, S. Ohno, and J. Fujikata, "III–V/Si Hybrid MOS Optical Phase Shifter for Si Photonic Integrated Circuits," J. Light. Technol., vol.37, no.5, pp.1474–1483, March 2019.
[13] C. Haffner, D. Chelladurai, Y. Fedoryshyn, A. Josten, B. Baeuerle, W. Heni, T. Watanabe, T. Cui, B. Cheng, S. Saha, D.L. Elder, L.R. Dalton, A. Boltasseva, V.M. Shalaev, N. Kinsey, and J. Leuthold, "Low-loss plasmon-assisted electro-optic modulator," Nature, vol.556, no.7702, pp.483–486, April 2018.
[14] C. Wang, M. Zhang, B. Stern, M. Lipson, and M. Lončar, "Nanophotonic lithium niobate electro-optic modulators," Opt. Express, vol.26, no.2, pp.1547–1555, Jan. 2018.
[15] S. Yokoyama, G.-W. Lu, H. Miura, Q. Feng, and A.M. Spring, "96 Gbit/s PAM-4 Generation using an Electro-Optic Polymer Modulator with High Thermal Stability," Conference on Lasers and Electro-Optics, San Jose, California, p.SM3B.2, 2018.
[16] Q. Xu, B. Schmidt, S. Pradhan, and M. Lipson, "Micrometre-scale silicon electro-optic modulator," Nature, vol.435, no.7040, pp.325–327, May 2005.
[17] X. Wu, C. Huang, K. Xu, C. Shu, and H.K. Tsang, "128-Gb/s Line Rate OFDM Signal Modulation Using an Integrated Silicon Microring Modulator," IEEE Photon. Technol. Lett., vol.28, no.19, pp.2058–2061, Oct. 2016.
[18] H. Li, B. Casper, G. Balamurugan, M. Sakib, J. Sun, J. Driscoll, R. Kumar, H. Jayatilleka, H. Rong, and J. Jaussi, "A 112 Gb/s PAM4 Silicon Photonics Transmitter with Microring Modulator and CMOS Driver," J. Light. Technol., vol.38, no.1, pp.131–138, Jan. 2020.
[19] T. Baba, H.C. Nguyen, N. Yazawa, Y. Terada, S. Hashimoto, T. Watanabe, "Slow-light Mach–Zehnder modulators based on Si photonic crystals," Sci. Technol. Adv. Mat., vol.15, no.2, p.024602, 2014.
[20] Y. Terada, T. Tatebe, Y. Hinakura, and T. Baba, "Si Photonic Crystal Slow-Light Modulators with Periodic p–n Junctions," J. Light. Technol., vol.35, no.9, pp.1684–1692, May 2017.
[21] Y. Hinakura, Y. Terada, T. Tamura, and T. Baba, "Wide Spectral Characteristics of Si Photonic Crystal Mach-Zehnder Modulator Fabricated by Complementary Metal-Oxide-Semiconductor Process," Photonics, vol.3, no.2, p.17, April 2016.
[22] Y. Hinakura, H. Arai, and T. Baba, "64 Gbps Si photonic crystal slow light modulator by electro-optic phase matching," Opt. Express, vol.27, no.10, pp.14321–14327, May 2019.
[23] T. Tamura, K. Kondo, Y. Terada, Y. Hinakura, N. Ishikura, and T. Baba, "Silica-Clad Silicon Photonic Crystal Waveguides for Wideband Dispersion-Free Slow Light," J. Light. Technol., vol.33, no.14, pp.3034–3040, July 2015.
[24] H. Ito, Y. Terada, N. Ishikura, and T. Baba, "Hitless tunable WDM transmitter using Si photonic crystal optical modulators," Opt. Express, vol.23, no.17, pp.21629–21636, 2015.
[25] K. Hojo, Y. Terada, N. Yazawa, T. Watanabe, and T. Baba, "Compact QPSK and PAM modulators with Si photonic crystal slow-light phase shifters," IEEE Photon. Technol. Lett., vol.28, no.13, pp.1438–1441, 2016.
[26] R. Sarkissian and J. O'Brien, "Group index oscillations in photonic crystal waveguides," Appl. Phys. Lett., vol.105, no.12, p.121102, Sept. 2014.
[27] G.E. Ponchak, J. Papapolymerou, and M.M. Tentzeris, "Excitation of coupled slotline mode in finite-ground CPW with unequal ground-plane widths," IEEE Trans. Microw. Theory Techn., vol.53, no.2, pp.713–717, Feb. 2005.
[28] X. Tu, K.-F. Chang, T.-Y. Liow, J. Song, X. Luo, L. Jia, Q. Fang, M. Yu, G.-Q. Lo, P. Dong, and Y.-K. Chen, "Silicon optical modulator with shield coplanar waveguide electrodes," Opt. Express, vol.22, no.19, pp.23724–23731, Sept. 2014.
[29] H. Xu, X. Li, X. Xiao, Z. Li, Y. Yu, and J. Yu, "Bandwidth performances analysis for high-speed silicon depletion-mode modulator," Optical Fiber Communication Conference, San Francisco, California, no.Th2A.17, 2014.
[30] K. Kubota, J. Noda, and O. Mikami, "Traveling wave optical modulator using a directional coupler $LiNbO_3$ waveguide," IEEE J. Quantum Electron., vol.16, no.7, pp.754–760, July 1980.
[31] K. Kawano, T. Kitoh, O. Mitomi, T. Nozawa, and H. Jumonji, "A wide-band and low-driving-power phase modulator employing a Ti:$LiNbO_3$ optical waveguide at 1.5 μm," IEEE Photon. Technol. Lett., vol.1, no.2, pp.33–34, Feb. 1989.
[32] S.H. Lin and S.-Y. Wang, "High-throughput GaAs PIN electrooptic modulator with a 3-dB bandwidth of 9.6 GHz at 1.3 μm," Appl. Opt., vol.26, no.9, pp.1696–1700, May 1987.
[33] R.G. Walker, "High-speed III-V semiconductor intensity modulators," IEEE J. Quantum Electron., vol.27, no.3, pp.654–667, March 1991.
[34] N.A.F. Jaeger and Z.K.F. Lee, "Slow-wave electrode for use in compound semiconductor electrooptic modulators," IEEE J. Quantum Electron., vol.28, no.8, pp.1778–1784, Aug. 1992.
[35] J. Shin, S.R. Sakamoto, and N. Dagli, "Conductor Loss of Capacitively Loaded Slow Wave Electrodes for High-Speed Photonic Devices," J. Light. Technol., vol.29, no.1, pp.48–52, Jan. 2011.
[36] H. Yu and W. Bogaerts, "An Equivalent Circuit Model of the Traveling Wave Electrode for Carrier-Depletion-Based Silicon Optical Modulators," J. Light. Technol., vol.30, no.11, pp.1602–1609, June 2012.
[37] R. Ding, Y. Liu, Y. Ma, Y. Yang, Q. Li, A.E.-J. Lim, G.-Q. Lo, K. Bergman, T. Baehr-Jones, and M. Hochberg, "High-Speed Silicon Modulator With Slow-Wave Electrodes and Fully Independent Differential Drive," J. Light. Technol., vol.32, no.12, pp.2240–2247, June 2014.
[38] S. Galal and B. Razavi, "10-Gb/s limiting amplifier and laser/modulator driver in 0.18-μm CMOS technology," IEEE J. Solid-State Circuits, vol.38, no.12, pp.2138–2146, Dec. 2003.
[39] B.G. Lee, C.L. Schow, A.V. Rylyakov, J. Van Campenhout, W.M.J. Green, S. Assefa, F.E. Doany, M. Yang, R.A. John, C.V. Jahnes, J.A. Kash, and Y.A. Vlasov, "Demonstration of a Digital CMOS Driver Codesigned and Integrated With a Broadband Silicon Photonic Switch," J. Light. Technol., vol.29, no.8, pp.1136–1142, April 2011.
[40] H. Ramon, M. Vanhoecke, J. Verbist, W. Soenen, P. De Heyn, Y. Ban, M. Pantouvaki, J. Van Campenhout, P. Ossieur, X. Yin, and J. Bauwelinck, "Low-Power 56Gb/s NRZ Microring Modulator Driver in 28nm FDSOI CMOS," IEEE Photon. Technol. Lett., vol.30, no.5, pp.467–470, March 2018.
[41] A. Leven, F. Vacondio, L. Schmalen, S. ten Brink, and W. Idler, "Estimation of Soft FEC Performance in Optical Transmission Experiments," IEEE Photon. Technol. Lett., vol.23, no.20, pp.1547–1549, Oct. 15, 2011.

Yosuke Hinakura received his B.E. and M.E. degree from the Department of Electrical and Computer Engineering, Yokohama National University, Yokohama, Japan, in 2015 and 2017, respectively. He is currently working towards the Ph.D. degree in photonic crystal optical modulator at the same university. He is a member of the Japan Society of Applied Physics. He received three academic awards including JSAP presentation award and OECC best student paper award in 2019.

Hiroyuki Arai received the B.E. degree in Electrical and Electronic Engineering, M.E. and D.E. in Physical Electronics from Tokyo Institute of Technology in 1982, 1984 and 1987, respectively. After research associate in Tokyo Institute of technology, he joined Yokohama National University as lecturer in 1989. Now he is professor in Department of Electrical and Computer Engineering, Yokohama National University. He was visiting scholar at university of California, Los Angeles in 1997 and was visiting professor in 2005 and adjunct professor, 2012-2014, respectively, at Yonsei University, Seoul. He investigated microwave passive components for high power handling applications such as RF plasma heating in large Tokamaks. He developed a flat diversity antenna for mobile telephone terminal, a polarization diversity base station antenna for Japanese PDC systems, small base station antennas of In-building micro cellular system and DOA estimation for cellular system. He received the Young Engineers Award from the IEICE of Japan in 1989 and the "Meritorious Award on Radio" by the Association of Radio Industries and Businesses in 1997 for the development of polarization diversity antenna, in 2006 for the development of DOA estimation system, and in 2011 for the development of light weight phantom. He was editor-in-chief of IEICE Transactions on Communications, 2005-2007, and was chair of IEEE AP-S Japan Chapter, 2009-2010. He was associate editor of IEEE Transactions on Antennas and Propagation, 2011-2013, and chair of Technical Group on Antennas and Propagation of IEICE, 2013-2014. He is Fellow of IEEE and IEICE. He will serve general the chair of ISAP 2020, Osaka, Japan.

Toshihiko Baba received his B.E., M.E. and Ph.D. degrees all from the Division of Electrical and Computer Engineering, Yokohama National University, Japan, in 1985, 1987 and 1990, respectively. He became an Associate Professor and a Full Professor with Yokohama National University in 1994 and 2005, respectively. He has studied ARROW waveguides, VCSELs, microdisk lasers, photonic crystals (PCs) and Si photonics. His first demonstration includes PC-based slow-light waveguides with the dispersion engineering, high-speed modulators, beam steering device, nanolasers, biosensors and LEDs, and various Si photonics passive components including the sharp bend waveguide and arrayed waveguide grating. He is the author or co-author of more than 200 journal papers. He is a member of IEICE, JSAP, IEEE/Photonics, and OSA, and an Associate Member of the Science Council of Japan. He served as a vice president of JSAP from 2018–2020. He was the recipient of JSPS Award in 2005, IEEE/LEOS Distinguished Lecturer Award in 2006/2007, Ichimura Academic Award in 2012, and Education, Culture, Sports, Science Minister's Commendation in 2016.